Experimental Results and the Basic Thermodynamic Cycle of an Ejector Driven Microturbine Generator

Andrew P. Camacho*†, William Gardner, Ivan Wang, Jared Dunnmon, Stefan Pelekies, Hardy Shen, Justin Jaworski, Chris Gilmore
Graduate Research Assistant
Department of Mechanical Engineering
Duke University
Durham, NC 27708
Email: apc6@duke.edu

Jonathan Protz
Assistant Professor
Department of Mechanical Engineering
Duke University
Durham, NC 27708

This paper reports on the design, thermodynamic cycle, and experimental results of an ejector-driven micro turbine generator. For this cycle, an ejector, as opposed to a compressor, creates a pressure gradient to drive a turbine. When connected to a micro-generator and an ethanol vapor boiler, a power output of 7.5 mW is delivered to a resistive load of 300 Ω *at an angular velocity of 27,360 RPM.*

Nomenclature

A Area
σ Area Ratio
u Axial Velocity
ρ Density
η Efficiency
α Entrainment Ratio
h Enthalpy
F Force
A Area
$\dot{m}$ Mass flow rate
$\dot{M}$ Momentum flow rate
$\dot{W}$ Power
P Pressure
T Temperature
V Voltage
$()_d$ Discharge
$()_m$ Motive
$()_s$ Suction
$()_t$ Total, or turbine
$()_{fg}$ Vaporization

1 Introduction

The realization of a self-sustaining micro-turbine engine has remained elusive due to the many difficulties associated with the Brayton cycle at the MEMS scale. For example, minimum component efficiencies for the compressor and the turbine must be realized for a Brayton cycle to close and produce net work [1]. However, at small scales the efficiencies of these components are diminished due to many factors such as increased viscous effects associated low Reynolds numbers and fabrication constraints that dictate non-optimal geometries [2]. The realization of scale independent parameters such as tip speed is also problematic at the MEMS scale. For example, to reach sufficient tip speeds and operate at a high turbine effectiveness requires extremely high rotor speeds; this can only be achieved with gas bearings [3]. These bearing systems however are difficult to implement in an integrated fashion at the MEMS scale. For micro-turbomachinery, hydrostatic bearing operation has so far always required an external, turbo-machine independent pressure source, and hydrodynamic bearing operation inherently experiences difficulties during the transient startup period that is associated with low rotor speeds [4]. Lastly, manufacturing micro-turbomachinery components at these scales with the required tolerances for the gas bearings poses technical challenges, as the surface roughness of the rotor walls

*Address all correspondence related to ASME style format and figures to this author.
†Address all correspondence for other issues to this author.

must remain well below the bearing clearance which is often in the range of 15 μm [5]. All of these obstacles make it difficult to appropriately implement a stand-alone self-sustaining Brayton cycle micro heat-engine.

This paper presents an alternative thermodynamic cycle that offers solutions to these challenges. This cycle is designed around static pumping devices, an injector and an ejector [6]. Both are based on the same fundamental principle as shown in figure 1: a high momentum motive fluid is mixed with a low momentum suction fluid, resulting in a discharge fluid with less overall momentum and thus a higher pressure. When discharged to ambient pressure conditions then, a sub-ambient pressure environment must exist upstream of the diffuser and mixing region, allowing fluid to be drawn in from ambient pressure. A turbine can then be placed in this flow path to produce work. For this cycle then, the ejector is used to create a pressure gradient across the turbine and hydrostatic gas bearings, while the injector pumps liquid into a high pressure boiler. The benefit of these components lies in their static and turbo-machine independent operation. Unlike a turbo-compressor, the ejector is uncoupled from the turbine and thus provides a pressure gradient across the turbine and gas bearings regardless of the turbine's rotor speed so long as heat is applied to the boiler. This eliminates many problems associated with the startup phase by removing the need for an external pressure source and guarantees that the cycle will close at any operating efficiency. In addition, because there are no moving parts associated with these pumping components, they can be more easily fabricated as their manufacturing tolerances are not as critical as those associated with rotating micro-turbomachinery components.

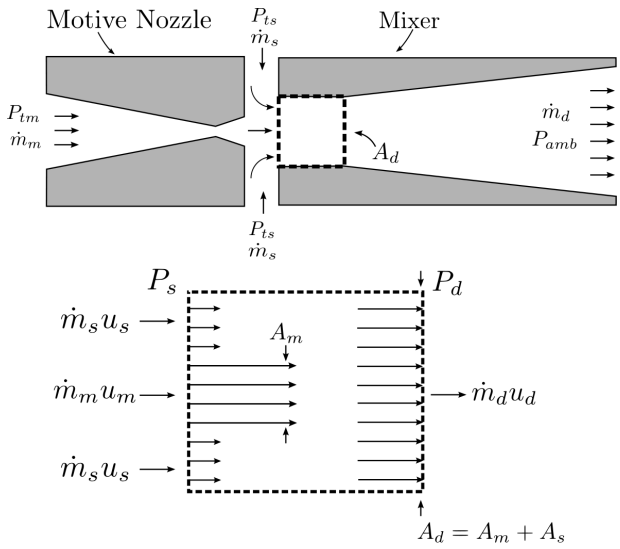

Fig. 1. Ejector assembly, flow paths, and mixing region control volume

This paper will discuss both the thermodynamic model concerning this type of cycle and the preliminary experimental results of an ejector-driven micro-turbo generator.

2 Thermodynamic Cycle

The proposed cycle, shown in figure 2, is derived from a steam locomotive cycle and an afterburning Brayton cycle. Combustion takes place downstream of the turbine, and the generated heat is split between preheating the turbine inlet air with the use of a recuperator and vaporizing the motive fluid in the boiler. The power from the turbine can be estimated from an incompressible flow assumption, the ideal gas law, and by recalling that the total pressure at the turbine inlet is roughly equal to ambient pressure.

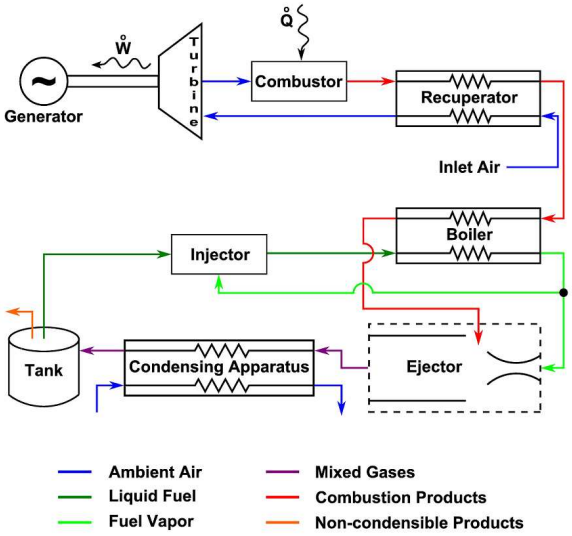

Fig. 2. A schematic of an afterburning thermodynamic cycle driven by an ejector

$$\frac{\dot{W}_t}{\dot{m}_s} = \eta_t \frac{\Delta P_t}{\rho} \approx \eta_t \frac{P_{amb} - P_{s,t}}{P_{amb}} R_{air} T_{t4} \tag{1}$$

The pressure difference between the ambient and total suction pressure can be determined by the conservation of mass and momentum from the control volume shown in figure 1, and by assuming isentropic expansion in the diffuser such that the exit dynamic head is approximately zero. As shown in appendix A, the result is

$$\frac{P_{amb} - P_{s,t}}{\frac{1}{2}\rho u^2} = \sigma \left[2 - \sigma(1+2\alpha) - \frac{\alpha^2 \sigma^3}{(1-\sigma)^2} \right] \tag{2}$$

where σ is the area ratio and α is the ejector entrainment ratio.

$$\sigma \equiv \frac{A_m}{A_d} \qquad \alpha \equiv \frac{\dot{m}_s}{\dot{m}_m} \tag{3}$$

The system rejects heat with the ejector discharge flow and by the cooling and condensation of the motive vapor.

However, the heat rejected in condensation typically far exceeds the heat rejected from the cooling of the exhaust gases. As such, the overall thermal efficiency of the cycle can be approximated as

$$\eta \approx \frac{\dot{W}_t}{\dot{W}_t + \dot{m}_m h_{fg}} \tag{4}$$

In addition, by further assuming that the turbine power is significantly less than the rejected heat, we can re-approximate the cycle efficiency as

$$\eta \approx \frac{\dot{W}_t}{\dot{m}_m h_{fg}} \tag{5}$$

Combining these equations we obtain

$$\eta = \frac{\eta_t R_{air} T_{t4} \alpha\sigma \left[2 - \sigma(1+2\alpha) - \frac{\alpha^2\sigma^3}{(1-\sigma)^2}\right] \frac{1}{2}\rho u^2}{h_{fg} P_{amb}} \tag{6}$$

where σ, u, and T are design parameters set my geometry and material constraints. Assuming an entrainment ratio of α = 2, an area ratio of σ = 0.125, a turbine efficiency of 50%, water vapor as the working fluid, and neglecting condensation, we can approximate the overall cycle efficiency for different parameters as shown in table 1. Note that while the efficiencies are quite low, the advantage of this cycle lies in its simple operation and its ability to close at such low efficiencies as demonstrated by experimentation.

Table 1. Efficiency Approximations

Example #	$\frac{P_{boiler}}{P_s}$	T_{t4}	η
1	2	500 K	0.6%
2	3	750 K	1.6%

3 Experimental Results

An experiment was conducted to demonstrate that an ejector power by ethanol vapor could create a pressure gradient across a turbine and drive its attached micro-generator to deliver electrical power. The turbine was originally designed and micro-machined as a radial flow impulse turbine with an NGV outer-diameter of 10 mm and blade heights of 250 μm as shown in figure 3. Details of its fabrication can be seen in appendix B. The ejector was micro-machined with a throat diameter of 733 μm, an area ratio of $\sigma = 0.125$ and was driven by ethanol vapor from a conventionally-sized boiler. More details on the ejector and its fabrication can be found in appendix B. The turbine was bonded to a 3-phase Faulhaber 1202-H-006-BH permanent magnet motor with a phase to phase internal resistance of 70Ω. The micro-engine can be seen in figure 4. We believe however that, due to the configuration and choice of materials, eddy current losses in the surrounding turbine NGV copper layer prevented the turbine from operating at its design rotor speed with a commensurate reduction in system performance. The results from the operation of this engine can be seen in table 2.

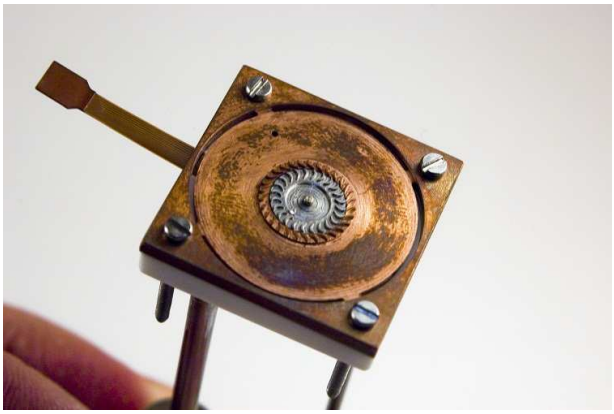

Fig. 3. A cross section of the original micro-turbine bonded to the rotor of a permanent magnet generator with protruding leads

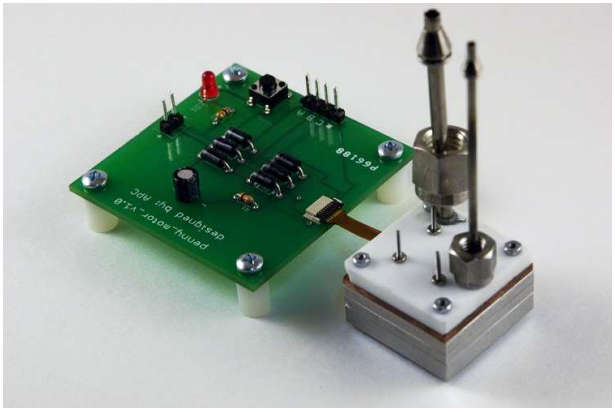

Fig. 4. The original micro-turbogenerator connected to power electronics (boiler and ejector not shown)

In order to achieve an RPM closer to the design speed of the turbine, a new turbine with an outer diameter of 11 mm and blade heights of 750 μm was 3D printed out of ABS plastic with a Dimension 1200es Series printer. For these experiments, the AC output from the micro-generator was rectified to DC with the use of 1N5817 Schottky diodes in a full-wave bridge configuration. This micro-turbogenerator can be seen in figure 5, and the results from the operation of this engine can be seen in table 3. Power from the engine was sufficient to light a row of LEDs as shown in figure 6.

Note that the maximum power is not achieved by setting the load resistance equal to the equivalent stator resistance as prescribed by the maximum power transfer theory. This can

Table 2. Experimental results of the first micro-turbogenerator

Property	Units	Value
Rotor Speed	RPM	5,505
Turbine Pressure Ratio	-	1.13
Mass Flow	g/s	2.40
Turbine Inlet Temp.	K	293
V_{RMS}	mV	180
Power	mW	2.94

Table 3. Experimental results of the 3D printed micro-turbogenerator

Property	Units	Value
Rotor Speed	RPM	27,360
Turbine Pressure Ratio	-	1.05
Boiler Pressure	atm	15
Turbine Inlet Temp.	K	293
V_{DC}	mV	1.49
Power	mW	7.5

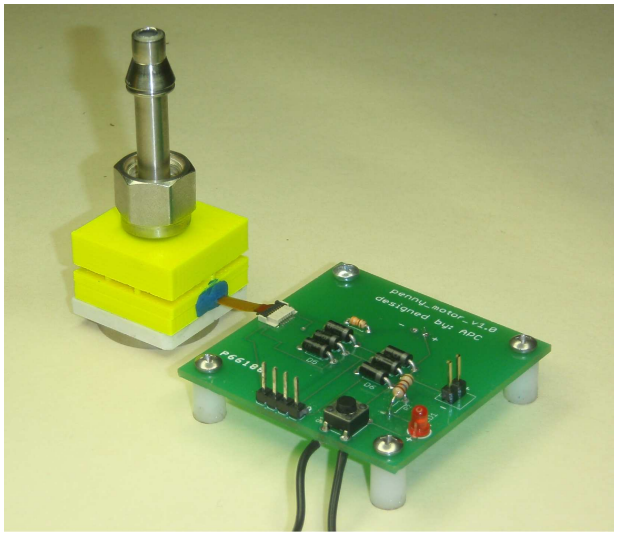

Fig. 5. The 3D printed micro-turbogenerator connected to the power electronics (boiler and ejector not shown)

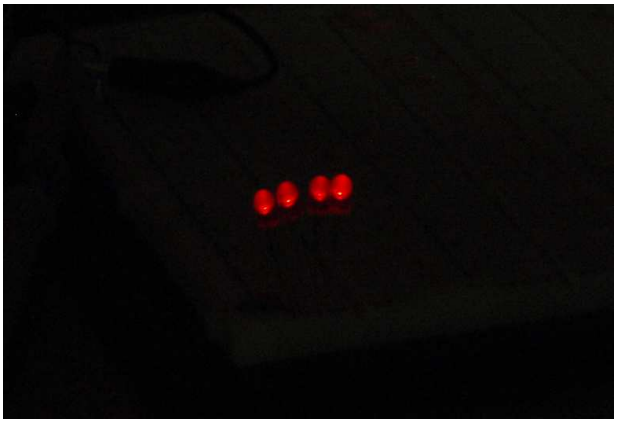

Fig. 6. LEDs powered by the boiler fed ejector driven micro-turbogenerator

be reasoned out quite simply. The maximum power transfer theorem assumes an electric circuit with an ideal voltage source. However, a turbo-generator outputs a variable voltage that is dependent upon RPM, and the shaft power output of the turbine also directly depends upon RPM. In particular, for a turbine operating under fixed thermodynamic conditions, there will be a design RPM which maximizes its shaft power output [7]. Combining these observations as shown in figure 7, it becomes quite obvious that the load resistance should be set to a value (R_2) that maximizes the shaft power output of the turbine. If instead the load resistance is set to the value prescribed by the maximum power transfer theorem (R_1), then the turbine will not be capable of achieving its design RPM, and the resultant power output will be lowered. In other words, if at the design RPM the electric circuit requires more power than the turbine can provide given its thermodynamic operating conditions, the turbine will decelerate and the overall power output will decrease.

4 Conclusion

This paper has proposed a power cycle designed around an ejector, a jet pump with no moving parts. In this cycle, the ejector is used, in lieu of a compressor, to produce a pressure gradient to drive a micro-turbogenerator and produce electrical power. An advantage of this operating cycle is that, unlike a standard Brayton cycle, there is no minimum required efficiency for the cycle to close and the engine to function, as demonstrated by the experimental results. The manufacturing tolerances of these static pumping devices are also much less stringent than silicon, gas bearing supported micro-turbomachinery, which greatly facilitates their fabrication and their operation in micro-heat engines. The thermodynamic cycle was analyzed with both compressible and incompressible flow assumptions, and a basic method of estimating the cycle thermal efficiency was presented. Experiments were conducted to demonstrate the viability of this ejector based power cycle for a micro-turbogenerator.

The use of an ejector also opens up the possibility for many different types of thermodynamic cycles. In addition to directly driving the turbine, the ejector could provide an easy means of creating the pressure gradient required by hydrostatic gas bearings. This could potentially allow for a fully integrated ejector/Brayton hybrid cycle that utilized an ejec-

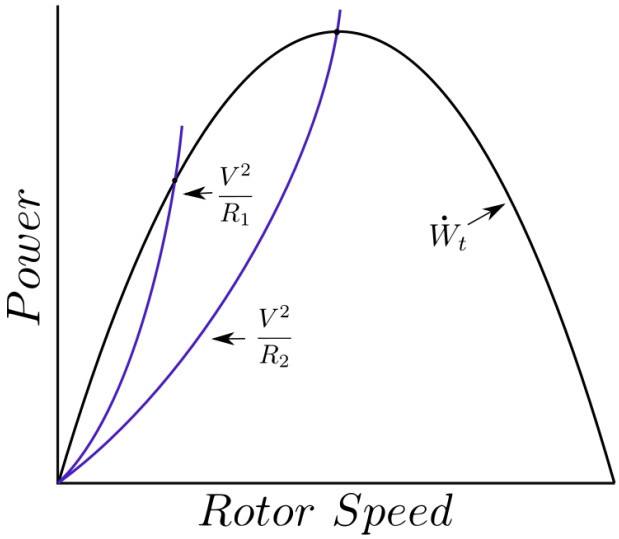

Fig. 7. Turbine shaft power and electric load power as a function of rotor speed

tor during the transient startup period associated with low RPM to power the gas bearings (in lieu of an external pressure source) and accelerate the turbomachinery. Once the turbomachinery was operating at sufficient RPM, the ejector portion of the cycle could be ceased, and the higher efficiency Brayton cycle could commence with bleed air from the compressor being used to power the gas bearings. A power turbine could also be used, allowing the turbomachinery and generator components to be uncoupled and to each operate at their own specific design RPM's, effectively simultaneously maximizing both the thermal and electric efficiencies. Such a cycle can be seen in figure 8.

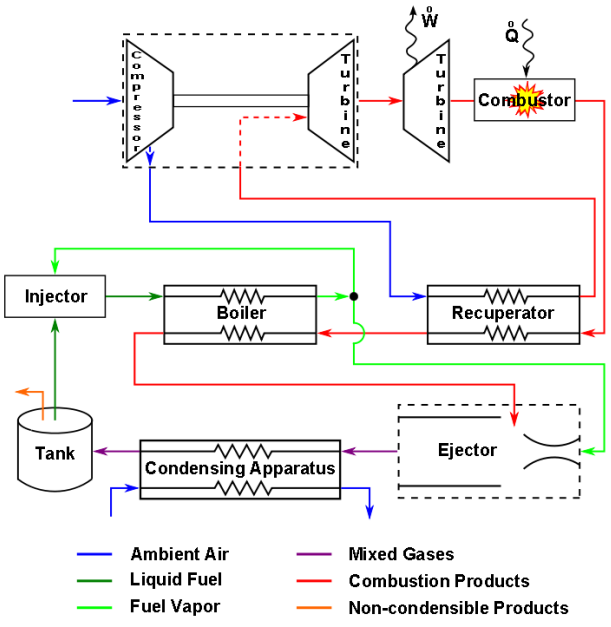

Fig. 8. A Brayton/ejector recuperated hybrid cycle utilizing a power turbine

References

[1] Kerrebrock, J. L., 1992. *Aircraft Engines and Gas Turbines*, 2nd ed. The MIT Press, Cambridge, Massachusetts.

[2] Lee, C., Arslan, S., and Fréchette, L., 2008. "Design Principles and Measured Performance of Multistage Radial Flow Microturbomachinery at Low Reynolds Numbers". *Journal of Fluids Engineering*, **130**, p. 111103.

[3] Liu, L. X., Teo, C. J., Epstein, A. H., and Spakovszky, Z. S., 2005. "Hydrostatic gas journal bearings for microturbomachinery". *Journal of Vibration and Acoustics*, **127**(2), pp. 157–164.

[4] Teo, C., and Spakovszky, Z., 2006. "Modeling and experimental investigation of micro-hydrostatic gas thrust bearings for micro-turbomachines". *Journal of turbomachinery*, **128**, p. 597.

[5] Teo, C., Liu, L., Li, H., Ho, L., Jacobson, S., Ehrich, F., Epstein, A., and Spakovszky, Z., 2009. "High-speed operation of a gas-bearing supported mems-air turbine". *Journal of Tribology*, **131**, July.

[6] Gardner, W., Wang, I., Jaworski, J., Brikner, N., and Protz, J., 2010. "Experimental investigation and modeling of scale effects in jet ejectors". *Journal of Micromechanics and Microengineering*, **20**, p. 085027.

[7] Shepherd, D. G., 1956. *Principles of Turbomachinery*. MacMillan Publishing Company, New York.

[8] Greitzer, E. M., Tan, C. S., and Graf, M. B., 2004. *Internal Flows: Concepts and Applications*. Cambridge University Press, Cambridge, UK.

[9] Shapiro, A. H., 1953. *The Dynamics and Thermodynamics of Compressible Fluid Flow*, Vol. 1. The Roland Press Company, New York.

A Ejector Model Derivation

This section shows the derivation for the ejector performance. The model is created by applying the conservation of mass and momentum across a constant area mixing duct as shown in figure 1, assuming incompressible flow in the mixing duct and diffuser, and assuming isentropic expansion in the downstream diffuser such that all of the dynamic head is converted to static pressure. The diffuser discharges to ambient conditions. The fluid densities are approximated as equal and constant by assuming similar gas temperatures upon mixing and incompressible flow in the mixing region. These assumptions simplify the analytical results; however the same fundamental laws and procedures can be used to numerically derive the result even when this is not the case. Doing so however sheds no light on the underlying mechanisms and does not clearly show the general relationship between the input variables and the output, which is the same in either case.

A.1 Conservation of Mass

The conservation of mass states that the total mass entering the control volume must equal the mass leaving the

control volume.

$$\dot{m}_m + \dot{m}_s = \dot{m}_d \tag{7}$$

Utilizing $\dot{m} = \rho u A$ and assuming incompressible flow this can be transformed into

$$u_m A_m + u_s A_s = u_d A_d \tag{8}$$

Noting that by geometry $A_m + A_s = A_d$, and defining an area ratio $\sigma \equiv \frac{A_m}{A_d}$, equation 8 becomes

$$u_m \sigma A_d + u_s (1-\sigma) A_d = u_d A_d \tag{9}$$

So the exit velocity as a function of geometry and inlet parameters is

$$u_d = u_m \sigma + u_s (1-\sigma) \tag{10}$$

A.2 Conservation of Momentum in the Mixing Region

From the conservation of axial momentum in the control volume we have

$$\dot{M}_{in} + \sum F = \dot{M}_{out} \tag{11}$$

Where

$$\dot{M}_{in} = \rho u_m^2 A_m + \rho u_s^2 A_s \tag{12}$$

$$\dot{M}_{out} = \rho u_d^2 A_d \tag{13}$$

Assuming uniform pressure in the y direction at both the inlet and outlet faces [8], and using geometry to equate the areas gives

$$\sum F = P_m A_m + P_s A_s - P_d A_d = A_d (P_s - P_d) \tag{14}$$

Plugging back the relations from equations 12-14 into 11 gives

$$\rho \left(u_m^2 A_m + u_s^2 A_s\right) + A_d (P_s - P_d) = \rho u_d^2 A_d \tag{15}$$

Dividing equation 15 through by A_d gives

$$\rho \left(u_m^2 \frac{A_m}{A_d} + u_s^2 \frac{A_s}{A_d} \right) + P_s - P_d = \rho u_d^2 \tag{16}$$

A.3 Non-dimensionalized total pressure difference

By utilizing the previously defined area ratio, σ, and substituting in equation 10, our result from the conservation of mass, equation 16 becomes

$$\rho \left[u_m^2 \sigma + u_s^2 (1-\sigma)\right] + P_s - P_d = \rho \left[u_m \sigma + u_s (1-\sigma)\right]^2 \tag{17}$$

When expanded and solved for $P_d - P_s$, this becomes

$$P_d - P_s = \rho\sigma u_m^2 + \rho\sigma u_s^2 - \rho\sigma^2 u_m^2 - \rho\sigma u_s^2 + 2\rho u_m u_s \sigma(\sigma - 1) \tag{18}$$

This represents the static pressure increase in the mixing area as a result of the mixing process. In order to assist in the non-dimensionalization of the final result, it is useful to divide equation 18 out by the motive vapor dynamic head, $\frac{1}{2}\rho u_m^2$. Doing so gives

$$P_d - P_s = \frac{1}{2}\rho u_m^2 \left[2\sigma + 2\sigma \frac{u_s^2}{u_m^2} - 2\sigma^2 - 2\sigma^2 \frac{u_s^2}{u_m^2} + 4\frac{u_s}{u_m}\sigma(\sigma - 1) \right] \tag{19}$$

This result can be further simplified as follows. From the conservation of mass we have

$$u_m = \frac{\dot{m}_m}{\rho A_m} \qquad \textit{and} \qquad u_s = \frac{\dot{m}_s}{\rho A_s} \tag{20}$$

Taking the ratio of these two results, recalling the entrainment ratio, $\alpha \equiv \frac{\dot{m}_s}{\dot{m}_m}$, and noting that the area ratio can be re-arranged to $\frac{A_m}{A_s} = \frac{\sigma}{1-\sigma}$, this becomes

$$\frac{u_s}{u_m} = \frac{\dot{m}_s A_m}{\dot{m}_m A_s} = \alpha \frac{A_m}{A_s} = \alpha \frac{\sigma}{1-\sigma} \tag{21}$$

Plugging equation 21 back into equation 19 and simplifying results in

$$P_d - P_s = \frac{1}{2}\rho u_m^2 2\sigma \left[1 + \alpha^2 \left(\frac{\sigma}{1-\sigma}^2 \right) - \sigma - \frac{\alpha^2\sigma^3}{(1-\sigma)^2} + \frac{2\alpha\sigma^2}{1-\sigma} - \frac{2\alpha\sigma}{1-\sigma} \right] \tag{22}$$

However, the ultimate goal is to determine the difference in total pressure, therefore the suction head is subtracted from both sides of the equation.

$$P_d - P_{s,t} = \frac{1}{2}\rho u_m^2 2\sigma \left[1 + \alpha^2 \left(\frac{\sigma}{1-\sigma} \right)^2 - \sigma - \frac{\alpha^2\sigma^3}{(1-\sigma)^2} + \frac{2\alpha\sigma^2}{1-\sigma} - \frac{2\alpha\sigma}{1-\sigma} \right] - \frac{1}{2}\rho u_s^2 \tag{23}$$

Utilizing equation 21 once again this becomes

$$P_d - P_{s,t} = \frac{1}{2}\rho u_m^2 \left(2\sigma \left[1 + \alpha^2 \left(\frac{\sigma}{1-\sigma} \right)^2 - \sigma - \frac{\alpha^2\sigma^3}{(1-\sigma)^2} + \frac{2\alpha\sigma^2}{1-\sigma} - \frac{2\alpha\sigma}{1-\sigma} \right] - \alpha^2 \left[\frac{\sigma}{1-\sigma} \right]^2 \right) \quad (24)$$

The static discharge pressure at the exit of the device however will come from isentropically expanding the mixing region exit flow enough such that its exit dynamic head is approximately zero. And from subsonic compressible flow laws [9], we know that the static exit pressure must be equal to ambient pressure. Thus

$$P_{amb} = P_d + \frac{1}{2}\rho u_d^2 \quad (25)$$

As such

$$\begin{aligned} P_{amb} - P_{s,t} &= P_d - P_{s,t} + \frac{1}{2}\rho u_d^2 \\ &= \frac{1}{2}\rho u_m^2 \left(2\sigma \left[1 + \frac{\alpha^2\sigma^2}{(1-\sigma)^2} - \sigma - \frac{\alpha^2\sigma^3}{(1-\sigma)^2} + \frac{2\alpha\sigma^2}{1-\sigma} - \frac{2\alpha\sigma}{1-\sigma} \right] - \alpha^2 \left[\frac{\sigma}{1-\sigma} \right]^2 \right) + \frac{1}{2}\rho u_d^2 \end{aligned} \quad (26)$$

Utilizing the mass conservation result, equation 10, this becomes

$$\begin{aligned} P_{amb} - P_{s,t} = & \\ & \frac{1}{2}\rho u_m^2 \left(2\sigma \left[1 + \frac{\alpha^2\sigma^2}{(1-\sigma)^2} - \sigma - \frac{\alpha^2\sigma^3}{(1-\sigma)^2} + \frac{2\alpha\sigma^2}{1-\sigma} - \frac{2\alpha\sigma}{1-\sigma} \right] - \frac{\alpha^2\sigma^2}{(1-\sigma)^2} \right) \\ & + \frac{1}{2}\rho u_m^2 \left(\sigma^2 + 2\frac{u_s}{u_m}\sigma - 2\frac{u_s}{u_m}\sigma^2 + \frac{u_s^2}{u_m^2} - 2\frac{u_s^2}{u_m^2}\sigma + \frac{u_s^2}{u_m^2}\sigma^2 \right) \end{aligned} \quad (27)$$

Utilizing equation 21 again and dividing through by the inlet dynamic head results in

$$\begin{aligned} \frac{P_{amb} - P_{s,t}}{\frac{1}{2}\rho u_m^2} = & \\ & 2\sigma \left[1 + \frac{\alpha^2\sigma^2}{(1-\sigma)^2} - \sigma - \frac{\alpha^2\sigma^3}{(1-\sigma)^2} + \frac{2\alpha\sigma^2}{1-\sigma} - \frac{2\alpha\sigma}{1-\sigma} \right] - \\ & \frac{\alpha^2\sigma^2}{(1-\sigma)^2} + \sigma \left[\sigma + \frac{2\alpha\sigma}{1-\sigma} - \frac{2\alpha\sigma^2}{1-\sigma} + \frac{\alpha^2\sigma}{(1-\sigma)^2} - \frac{2\alpha^2\sigma^2}{(1-\sigma)^2} + \frac{\alpha^2\sigma^3}{(1-\sigma)^2} \right] \end{aligned} \quad (28)$$

Combining terms and simplifying, the final form of this equation, which was used in section 2, becomes

$$\frac{P_{amb} - P_{s,t}}{\frac{1}{2}\rho u_m^2} = \sigma \left[2 - \sigma(1+2\alpha) - \frac{\alpha^2\sigma^3}{(1-\sigma)^2} \right] \quad (29)$$

The 3D graph for this equation can be seen in figure 9. The results line up quite well with intuition. As an example, as the area ratio of the ejector approaches 1 and the entrainment ratio approaches 0, the device should begin to act more like an ideal isentropic diffuser. That is, the non-dimensionalized pressure increase should approach 1, as is shown in the figure, as all of the dynamic head is converted into pressure. Likewise, lower area ratio values are required to achieve higher entrainment ratios as one would expect.

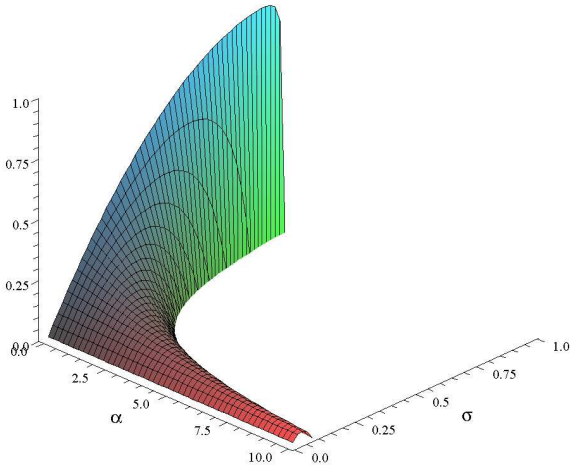

Fig. 9. Non-dimensionalized total pressure increase as a function of the area and entrainment ratios

B Fabrication

All metal test pieces were fabricated from either austenitic 303 stainless steel or machinable copper. For pieces in the direct vicinity of the magnetic rotor, these materials were chosen due to their non-magnetic properties. Ferromagnetic materials detrimentally interfered with the ball bearing system of the magnetic rotor and prevented rotation.

The axisymmetric nozzle and mixer were fabricated from 303 stainless steel using electrical discharge machining (EDM). All other pieces were fabricated using a Daewoo Doosan DMV 3016L 3-axis CNC mill with a maximum spindle speed of roughly 12,000 RPM. Feed rates were typically 0.001 inches per minute per flute and were initiated with a 0.0005 inch plunge. Carbide flat end mills and drill bits were supplied from either Drill Bit City (Chicago, IL) or Microcut (Kingston, MA) and plunged to depths less than 3x the tool diameter.

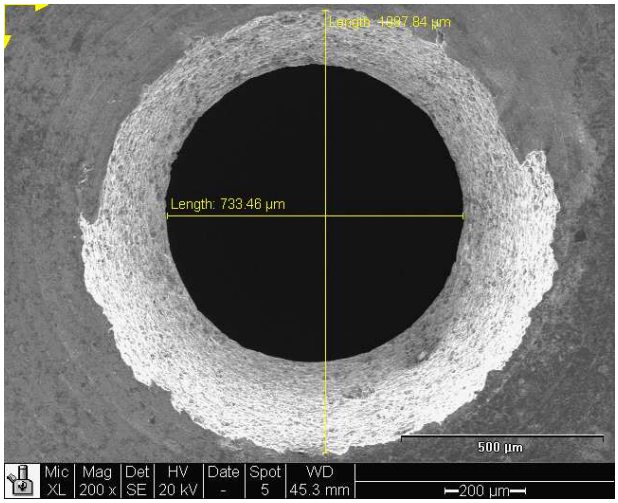

Fig. 10. Axisymmetric nozzle fabricated in 303 stainless steel using EDM showing realized dimensions

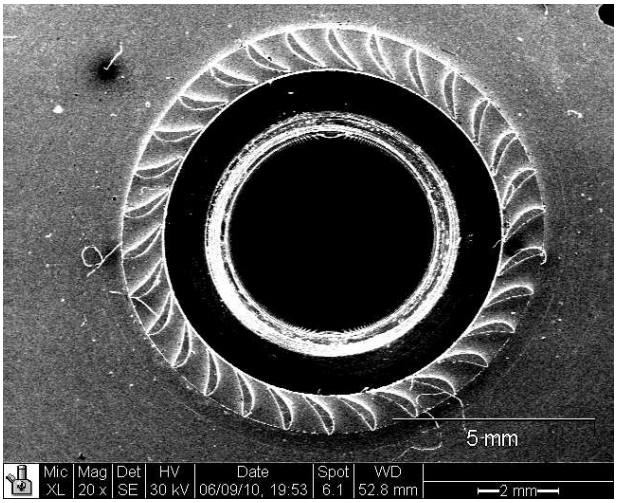

Fig. 12. The stator machines from machinable copper using CNC milling

The axisymmetric motive nozzle, shown in figure 10, was fabricated from 303 stainless steel using EDM. The realized throat width of 733 μm was roughly 20 μm or 3% smaller than design. The mixer and diffuser for the ejector were similarly fabricated from 303 stainless using EDM.

The turbine rotor for the test unit was fabricated from 303 stainless steel using an end mill and a 3 axis Daewoo Doosan DMV 3016L mill. The rotor appears in figure 11. The planar features (hub, shaft bore and blades) were milled

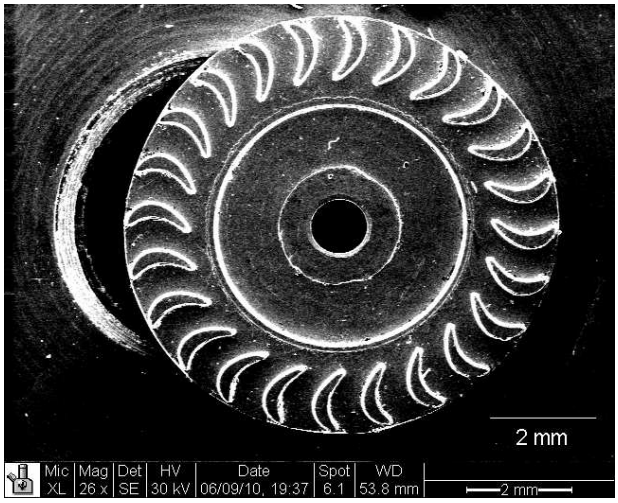

Fig. 11. The turbine rotor machined from 303 stainless steel using CNC milling

from a piece of sheet stock. The rotor outer wall was then machined by progressive surface milling operations around its perimeter, except for two punch out tabs, or struts, which remained to support the rotor prior to release. The punch out tabs were clipped, releasing the rotor, then manually sanded until visually flat. The turbine NGV's, shown in figure 12, were similarly fabricated from machinable copper. The rotor diameter was measured in 6 locations using Sylvac Micron Calipers. The design diameter was 7.898 mm with zero eccentricity and the realized diameter was 7.884 mm with an elliptical angular eccentricity of 0.081